Extracting Geometry and Topology of Orange Pericarps for the Design of Bioinspired Energy Absorbing Materials

Chelsea Fox, Kyle Chen, Micaela Antonini, Tommaso Magrini,* and Chiara Daraio*

As a result of evolution, many biological materials have developed irregular structures that lead to outstanding mechanical performances, like high stiffness-to-weight ratios and good energy absorption. However, reproducing these irregular biological structures in synthetic materials remains a complex design and fabrication challenge. Here, a bioinspired material design method is presented that characterizes the irregular structure as a network of building blocks, also known as tiles, and rules to connect them. Rather than replicating the biological structure one-to-one, synthetic materials are generated with the same distributions of tiles and connectivity rules as the biological material and it is shown that these equivalent materials have structure-to-property relationships similar to the biological ones. To demonstrate the method, the pericarp of the orange, a member of the citrus family known for its protective, energy-absorbing capabilities is studied. Polymer samples are generated and characterized under quasistatic and dynamic compression and display spatially-varying stiffness and good energy absorption, as seen in the biological materials. By quantifying which tiles and connectivity rules locally deform in response to loading, it is also determined how to spatially control the stiffness and energy absorption.

1. Introduction

Nature provides many examples of materials with desirable mechanical properties, such as high strength,[1–5] high toughness,[4,6–8] and high impact resistance.[2,9–12] Some of

C. Fox, K. Chen, T. Magrini, C. Daraio
Division of Engineering and Applied Science
California Institute of Technology
Pasadena, CA 91125, USA
E-mail: t.magrini@tue.nl; daraio@caltech.edu
M. Antonini
Department of Biotechnology and Life Sciences
University of Insubria
Varese 21100, Italy
T. Magrini
Department of Mechanical Engineering
Eindhoven University of Technology
Eindhoven 5600MB, The Netherlands

these materials are periodic, like nacre,[1,4] conch shells,[13] and beetle wings,[5] while others have irregular structures, like trabecular bone[2,9,10] and citrus pericarp.[14,15] However, periodic bioinspired materials are more widely studied than irregular materials, as they are more easily fabricated via additive manufacturing[16–22] and studied computationally.[18,19,21,23–25] Conversely, generating irregular materials often requires complex biomimicking processes, such as microcomputed tomography coupled with 3D printing,[26,27] or investment casting.[28,29] Other approaches include the use of stochastic processes, such as virtual growth algorithms (VGA),[30,31] Voronoi tessellations,[32–34] and foaming[35–40] for irregular materials generation, but these methods are limited in their ability to imitate the biological structure. Indeed, biological materials are often defined by highly complex and geometrically irregular concave and convex internal structures,[3,11,14,41,42] as well as spatial density variation, optimized to respond to specific loading conditions.[2,15,26,42,43]

Here, we propose a bioinspired material design method that characterizes the irregular biological structure by discretizing it into a network of tiles and rules for how to connect them. The set of available tiles and their connectivity rules lead to materials that, in a stochastic sense, have predetermined topology and geometry. Topology is defined as the connectivity between adjacent tiles, and we quantify it for each tile as the topological coordination number, R, defined as the number of branches connecting to neighbors from the central node.[44] Geometry is defined as the shape of elements in the structure, and is relevant at different scales: i) at the individual tile level and ii) after tessellation, at the structural feature level, consisting of assemblies of multiple tiles. Tiling and tessellation approaches that generate irregular geometries have already been studied to achieve mechanical properties such as stiffness and strength,[30,45–49] but these approaches often focus on homogenization or have very limited size due to computational costs,[50] whereas our approach seeks to quantify the structure and its structure-to-property relationships at a local tile level that can be spatially controlled and scaled.

To demonstrate the bioinspired material design method, we focus on the pericarp of the orange, a member of the citrus family.[41] Citrus fruits are known for their thick pericarps, which range from 5 to 7 mm for oranges and lemons, to 15–20 mm

**ADVANCED
SCIENCE NEWS**

www.advancedsciencenews.com

**ADVANCED
MATERIALS**

www.advmat.de

for the citron (the thickest pericarp).[51] Regardless of the type of fruit, these thick pericarps consist of an irregular, density-graded foam-like structure, which has evolved for energy absorption and impact resistance, key to protecting the pulp when the ripe fruit falls from the tree.[15,51] The dense outer layer of the pericarp, known as the flavedo, acts as a protective layer, while the less dense internal region, known as the albedo, provides energy absorption due to the presence of large, compressible intercellular spaces.[15] Furthermore, vascular bundles throughout the structure act as reinforcing elements, providing additional strength and stiffness.[15] We determine the tiles and connectivity rules of the orange pericarp and then use these as instructions for a computer-aided virtual growth algorithm[30] to generate equivalent synthetic samples with the same tile and connectivity rule distributions as the fruit, which we then additively manufacture. Under quasistatic and dynamic compression, we observe spatially-varying stiffness and energy absorption similar to that of the biological material, indicating that the tiles and connectivity rules are sufficient structural descriptors for the mechanical properties. We then quantify which tiles and connectivity rules produce a particular property by examining the local deformation to understand how to spatially control the mechanical performance.

1.1. Methods, Results, and Discussion

1.1.1. Bioinspired Material Design

We begin with a 2D cross-sectional image of an orange pericarp, acquired transversely from the external surface to approximately 5 mm into the fruit, where the pericarp transitions into the pulp (Figure S1, Supporting Information). We use the image processing software, FIJI,[52] to skeletonize[53] the structure into a simplified line form of the original pericarp image (**Figure 1**a). This irregular image skeleton is then broken down using a uniform square grid into a collection of tiles (Figure 1b,c). The tile size is determined by taking the largest possible size while ensuring that each tile contains no more than one node, defined here as an intersection point between branches (Figure 1b). Although each tile contains a unique portion of the original orange pericarp image, all tiles can be reduced to the simplest set of five tile types (Figure 1d). Each tile in the reduced set has the same branch thickness, which was chosen to match the volume fraction of the orange pericarp's structure, so that the branch length to thickness ratio is maintained when the tiles are assembled at any scale. We perform the translation process between the original tiles and the reduced tiles by analyzing the tile perimeter, counting the number branch intersections, and assigning a binary code value to the left (1), top (10), right (100), and bottom (1000), or zero otherwise (Figure 1d). By summing the perimeter values for each unique biological tile, we can determine its coordination number, as well as its orientation (Figure 1f; and Supporting Information Discussion 1). Next, we determine the connectivity rules governing how the tiles are assembled by examining the frequency at which two tiles are adjacent in the biological structure (Figure 1e,g; and Supporting Information Discussion 1). The frequency of the tiles and the rules that determine their connectivity, two parameters that can be extracted from any start-

ing structure (Figure 1h), are then supplied to a virtual growth algorithm[30] to assemble the irregular bioinspired structure (Figure 1i).

1.1.2. Material Generation and Fabrication

To generate samples, we divide the orange pericarp into external and internal regions, which correspond to the flavedo and the albedo,[15,41] respectively (**Figure 2**a–c). The external region is from 0 to 0.5±0.16 mm into the pericarp and the internal region is from 0.5±0.16 to 5 mm into the pericarp, where the endocarp and pulp begin. Using the gridded approach on eight different equivalent pericarp images (Figure S1, Supporting Information), we determine that the external region is composed of 20.6% ± 1.3% of coordination number zero (0-R) tiles, 34.8% ± 1.2% of coordination number two (2-R) tiles, 34.7% ± 1.4% of coordination number three (3-R) tiles, and 10.0% ± 1.0% of coordination number four (4-R) tiles (Figure 2d, blue). The internal region is composed of 26.6% ± 1.6% of 0-R tiles, 36.9% ± 1.3% of 2-R tiles, 28.2% ± 1.4% of 3-R tiles, and 8.3% ± 0.9% of 4-R tiles (Figure 2d, orange). Although all connectivity rules occur at some point in the original orange pericarp, the current virtual growth algorithm assembles tiles based on either allowed or disallowed connections. As such, to help with accurately capturing the geometry of the original sample and avoid defects during tessellation, we have a limit for when to keep or remove a connectivity rule. If the connectivity rule appears less than 5% of the time, it is automatically removed, while if it appears less than 15%, it is removed only if either of the two tile coordination types that make up the rule appear in other connectivity rules. In the external region, all connectivity rules are included except between 0-R tiles and 0-R tiles, and between 4-R tiles and 4-R tiles (Figure 2e, blue). In the internal region, all connectivity rules are included except between 3-R tiles and 4-R tiles, and 4-R tiles and 4-R tiles (Figure 2e, orange).

With the tile frequencies and connectivity rules extracted from the two different regions of the orange pericarp, a computer-aided virtual growth algorithm[30] uses the set of five tile types to generate 50×50 tile samples for the external (VGA-ext) and the internal (VGA-int) regions (Figure 2f,g). These samples are then combined together to form the bioinspired equivalent of the orange pericarp (VGA-full): a continuous structure with interface-free, spatially-varying density and structural features, defined as the areas enclosed by cell walls (Figure 2h). We 3D print the VGA-generated geometries into a two-phase composite material to create a structure suitable for mechanical testing, image analysis and strain mapping. We use a polyjet printer (Stratasys Objet500 Connex3), with a stiff viscoelastic resin (Stratasys VeroWhite Polyjet Resin) for the reinforcing structure, and a soft elastomeric resin (Stratasys TangoBlack Polyjet Resin) for the matrix, both of whose mechanical properties fall within those reported in literature.[54–56]

Although we exactly imitate the topology of the original sample by matching tile percentages, we must also quantify how well the VGA-generated samples' geometry compares with the original orange pericarp. For this, we use two different metrics: density, as a measure of structural feature size, and concavity, as a measure of structural feature shape. We observe that the
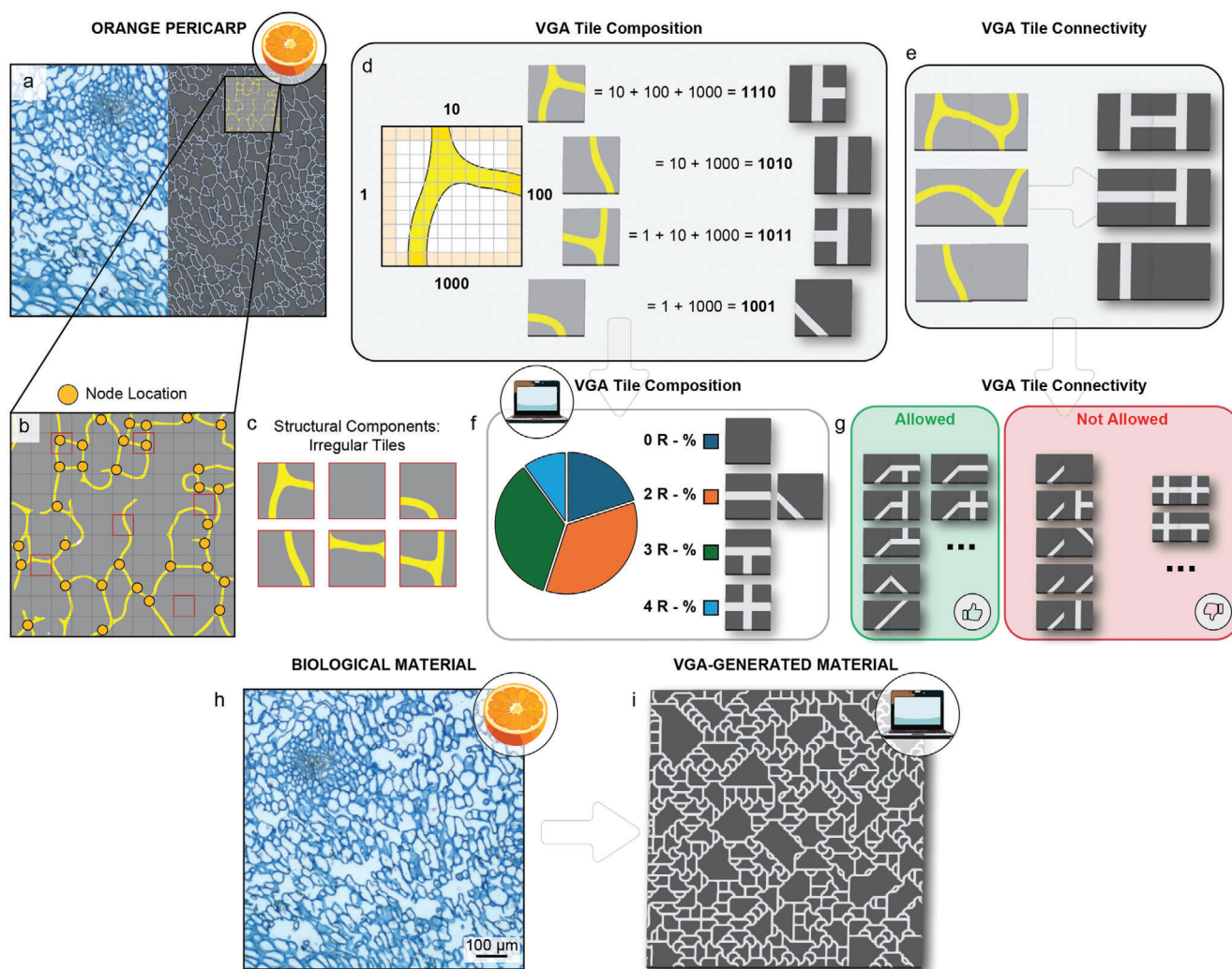
Figure 1. Bioinspired material design method. a) Orange pericarp image with right half as skeletonized structure. b) Skeletonized structure with node locations. c) Irregular biological tiles from skeleton. d) Translation of biological tiles into reduced tile types using perimeter identification numbers and summation. e) Connectivity rules from skeleton image. f) Reduced set of five VGA tiles and their coordination number, R. g) VGA-allowed and -not-allowed connectivity rules. h) Example image of orange pericarp. i) Example of VGA-generated sample.

VGA-generated samples maintain the same density difference between the external and internal regions as the orange pericarp samples, with 3%–5% lower density in the internal region as a result of the larger structural features (Figure 2i). To compare the concavity of the original samples with the VGA-generated samples, we examine each structural feature, using the bridge length to Euclidean distance ratio, where the bridge length is the length of a structural feature's edge between 3-R and 3-R or 4-R nodes, and the Euclidean distance is the linear distance between the 3-R and 3-R or 4-R nodes (Figure S2, Supporting Information). A ratio value of 1 indicates no concavity, whereas a higher ratio indicates a greater degree of concavity. When compared with the orange pericarp's structural features, the VGA-generated samples are very similar, with average concavity values within 2% for both regions, and with the internal region features having significantly higher concavity than the external region features (Figure 2j).

We also observe that the orange pericarp and the VGA-generated samples have an isotropic distribution of structural features, which can be shown by examining the orientation of the structural features averaged over several samples to determine how the features are distributed. Using the orientation of an elliptic fit in MATLAB (MathWorks, USA), we observe a uniform distribution of structural feature orientations in the internal region, while the distribution is more bimodal (0° and 180°) in the external region (Figure S3, Supporting Information). This bimodal distribution is due to the extensive presence of small, circular cells, but it is an artefact, as circular cells are inherently isotropic. Although the angles of orientation show a uniform distribution, they are not an independently sufficient metric to confirm an isotropic material distribution, because they do not consider the effect of feature size. Therefore, we also verify that the orientation angles do not correspond to a certain structural feature size to ensure isotropy. There is no correlation between size
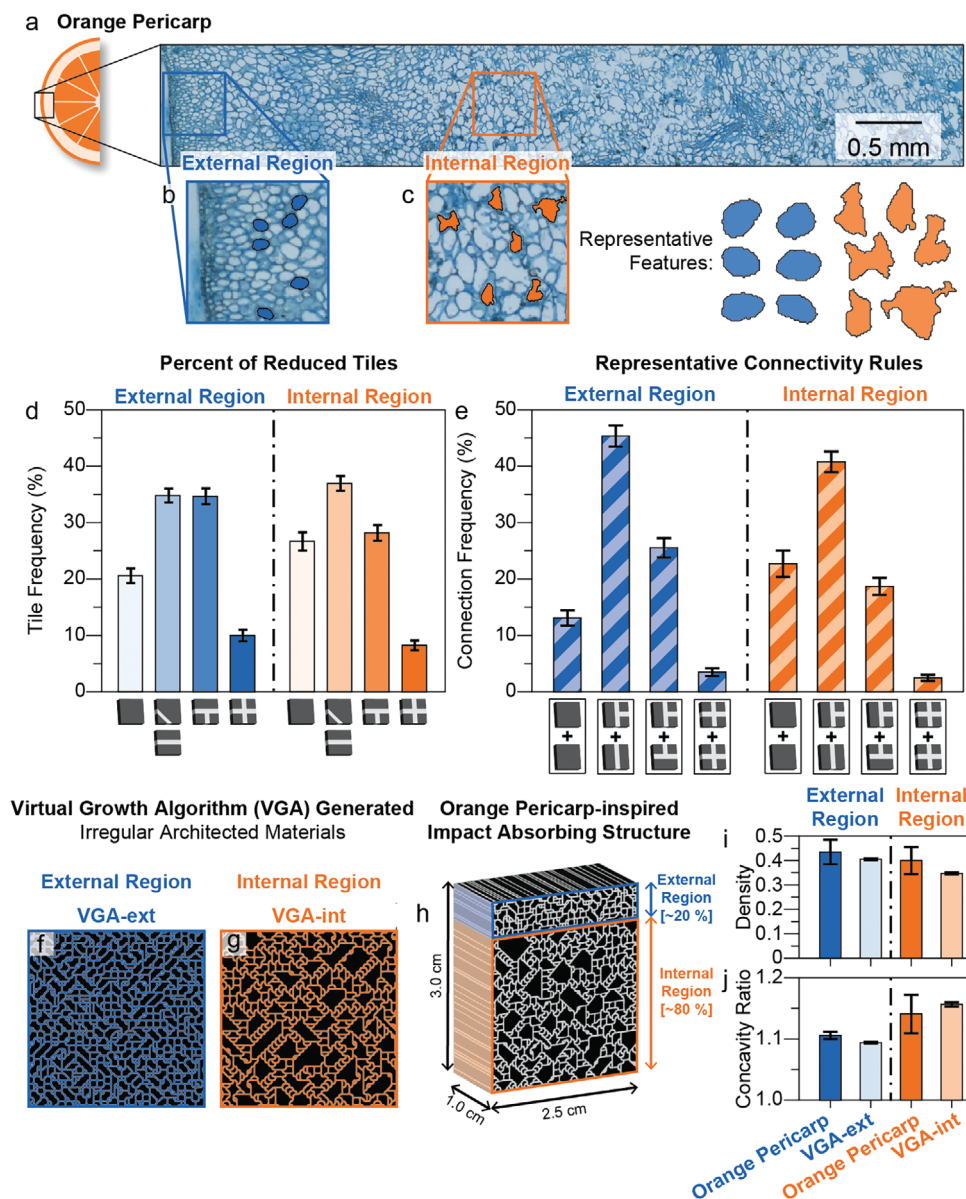
Figure 2. Orange pericarp characterization and VGA sample generation. a) Cross-sectional image of orange pericarp. b) Representative image of external region. c) Representative image of internal region. d) Tile percentages for external and internal regions. e) Selected connectivity rule percentages for external and internal regions. f) VGA-generated sample of external region. g) VGA-generated sample of internal region. h) 3D-printed composite polymer sample with 80% + 20% external and internal regions, respectively. i) External and internal region density for orange pericarp and VGA samples. j) External and internal region concavity ratio for orange pericarp and VGA samples.

and angle in the orange pericarp internal and external regions, or in the VGA-int samples, although there is a slight correlation for angles of 0°, 45°, 90°, and 135° in the VGA-ext samples, due to the four-sided nature of the virtual growth algorithm coupled with higher coordination number resulting in lower polydispersity (Figure S3, Supporting Information). Finally, it should be noted that the VGA-int samples individually are not isotropic because their mechanical response is dominated by a few of the largest features, due to testing size limitations (Figure S4, Supporting Information).

1.1.3. Mechanical Characterization: Quasistatic Testing

After establishing the topology and geometry equivalence of the VGA-generated samples with the original orange pericarp samples, we conduct quasistatic compression tests on additively manufactured polymer composite samples (Supporting Information Discussion 2). Like the original orange pericarp, which features a stiff, protective flavedo,[15,41] VGA-ext samples prove to be 116% stiffer than the VGA-int samples (**Figure 3a,b**, respectively) and even when normalized for their difference in density,

**ADVANCED
SCIENCE NEWS**

www.advancedsciencenews.com

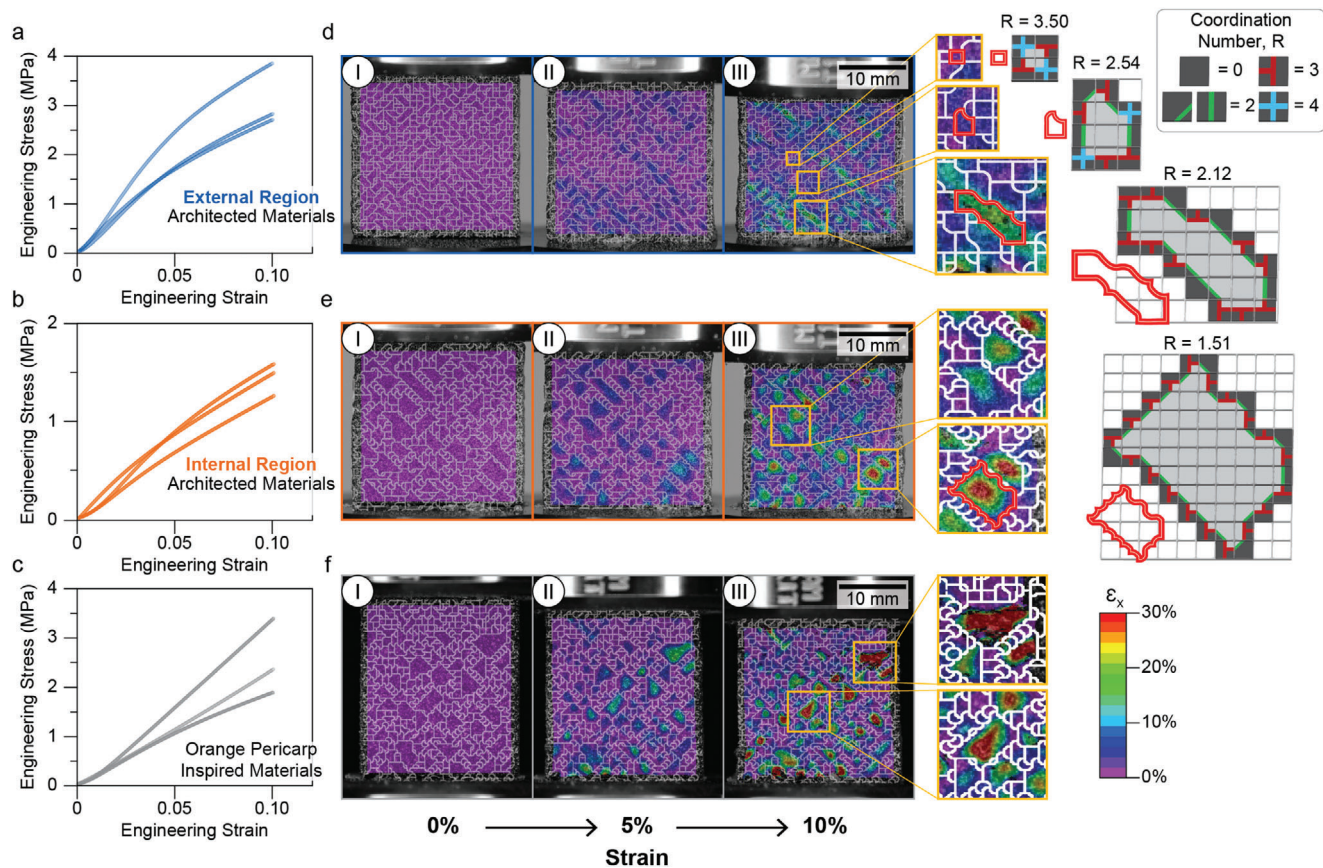**ADVANCED
MATERIALS**

www.advmat.de

Figure 3. Quasistatic compression tests. a) VGA-ext engineering stress–strain plot for three different samples. b) VGA-int engineering stress-strain plot for three different samples. c) VGA-full engineering stress–strain plot for three different samples. d) Example 2D DIC strain maps for 0%, 5%, and 10% global strain for VGA-ext sample, yellow insets show coordination color coded example structural features. e) Example 2D DIC strain maps for 0%, 5%, and 10% global strain for VGA-int sample, yellow insets show concave structural features at high strain and coordination color coded example structural feature. f) Example 2D DIC strain maps for 0%, 5%, and 10% global strain for VGA-full sample, yellow insets show concave structural features at high strain.

VGA-int samples prove more compliant, like the energy-absorbing albedo of the orange pericarp.[14,15,51] The orange pericarp inspired samples, VGA-full, featuring a 20% external and 80% internal composition, have a stiffness that is between the VGA-ext and VGA-int samples (Figure 3c). The constitutive stress–strain plots for VGA-full samples with a different composition, featuring 10% external and 90% internal, as well as 50% external and 50% internal, also have an intermediate stiffness (Figure S, Supporting Information). We also quantify which tiles and connectivity rules are primarily responsible for the stiffness variations by examining the local feature deformation. We do this by quantifying the strain field experienced by each sample up to 10% total strain, using 2D digital image correlation (2D DIC) to identify which features are the stiffest (and undergo the least deformation) and which features are the least stiff (and undergo the most deformation) (Figure 3d–f). We then break down these features into their constitutive tiles and connectivity rules and identify which tiles and rules appear in a feature, according to the amount of strain. 2D DIC shows that the strain field in VGA-ext samples is more uniformly distributed, with no region exceeding 15% local strain at a global strain of 10% (Figure 3, III) and that the samples are more homogenously composed of many smaller

stretching-dominated[31] structural features (Figure 3d), like the protective flavedo and reinforcing vascular bundles of the orange pericarp.[15] These features are formed by high percentages of high coordination tiles and by limiting large consecutive 0-R and 2-R tile connections, which results in lower polydispersity and local structural feature coordination numbers from ≈2 up to 3.5 (Figure 3d, III, insets). The local structural feature coordination number is calculated from the average of all tiles that compose a given structural feature.

In contrast, VGA-int samples display a significantly more localized strain field, with certain structural features reaching up to 30% local strain, although these local regions of high strain are uniformly distributed across the sample (Figure 3e, III, insets). This is in contrast to the periodic and graded honeycomb samples tested under the same loading conditions, which begin to form local shear bands (Figure S6, Supporting Information). We can observe that the VGA-int samples are composed of larger structural features, like the highly compressible, large intercellular spaces of the orange pericarp,[15] formed by higher percentages of low coordination tiles and large consecutive 0-R tile connections, as well as by consecutively aligned tiles (such as 2-R to 2-R, or 3-R to 3-R) or by consecutively repeating two-tile combinations (such
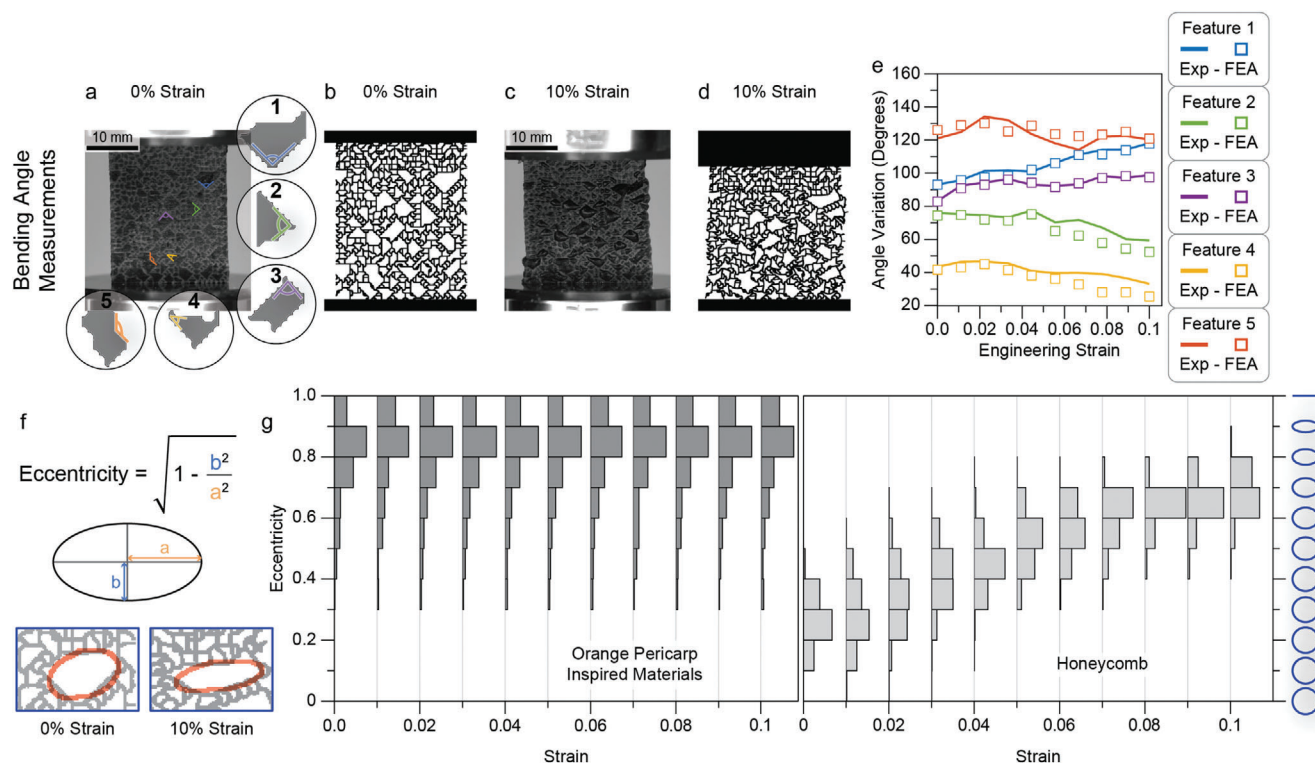
**ADVANCED
SCIENCE NEWS**

www.advancedsciencenews.com

**ADVANCED
MATERIALS**

www.advmat.de

Figure 4. Experimental and finite element analysis of changes in structural feature morphology under quasistatic compressive loading. a,c) Experimental testing of VGA-full structural features from 0% to 10% global strain, insets show example features with example bending angles. b,d) Finite element analysis of VGA-full reinforcing phase structural features from 0% to 10% global strain. e) Comparison of experimental and finite element analysis of variations in bending angle of example structural features from 0% to 10% global strain. f) Defining elliptic fit of structural features and their resulting eccentricity as a way to measure structural feature deformation. g) Tracking the eccentricity of all structural features from 0% to 10% global strain in the VGA-full reinforcing phase (left) and in honeycomb reinforcing phase (right).

as repetitions of the same 2-R to 3-R pair), which prevents the diversion of feature edges (Figure 3e, III, insets). This results in local coordination numbers as low as 1.5, allowing for less stiff bending and buckling mechanisms,[57] as well as higher polydispersity (Figure 3e, III, insets). Furthermore, the largest, most deformed structural features have many concave edges, formed by the connection of diagonal 2-R tiles with 3-R tiles, which act as less-constrained joints[58,59] that can rotate as the feature deforms (Figure 3e, III, insets). Finally, the VGA-full sample shows the same trends, with the internal region displaying highly localized strain values up to 30% (Figure 3f, III, insets), while the external region never exceeds 15% local strain.

1.1.4. Mechanical Characterization: Structural Feature Analysis

We conduct computational simulations of the samples using the COMSOL 2D linear elastic solid mechanics module to gain further understanding of the deformation mechanisms of the individual structural features and their effect on the global mechanical performance under compressive loading. To validate the computational results, we first manually track the bending angles of several structural features in the experimentally-tested VGA-generated samples (**Figure 4a,c**) using the image processing software, FIJI.[52] Although the experimental samples are composite materials, the simulated bending angle results on just the re-

inforcing phase are a close match because the matrix phase is significantly less stiff and does not play a significant role in the bending of features at low strain (Figure 4b,d,e). As the strain increases, the bending angles display varying changes, with some increasing, then decreasing, some remaining relatively constant, while yet others only increase or only decrease (Figure 4e). We then computationally study the distributions of all structural features in the samples using the eccentricity in MATLAB (Math-Works, USA) from elliptic fits of each feature as a proxy for bending angle (Figure 4f,g, left). We observe that the distribution of eccentricities remains similar across all strains, the result of some features becoming more elongated while others become more circular with increasing strain, making the material locally anisotropic but globally isotropic (Figure 4g, left). This is in contrast to the honeycomb, whose distribution shifts up (Figure 4g, right) as every feature becomes more elongated with increasing strain.

1.1.5. Mechanical Characterization: Dynamic Testing

To characterize the energy absorption capabilities of the VGA-generated samples, drop tower tests at a strain rate of ≈100 s^{-1} are conducted. To quantify the energy absorption capabilities of the VGA-generated materials, we measure the time of contact between the striker and sample, and the coefficient of restitution,
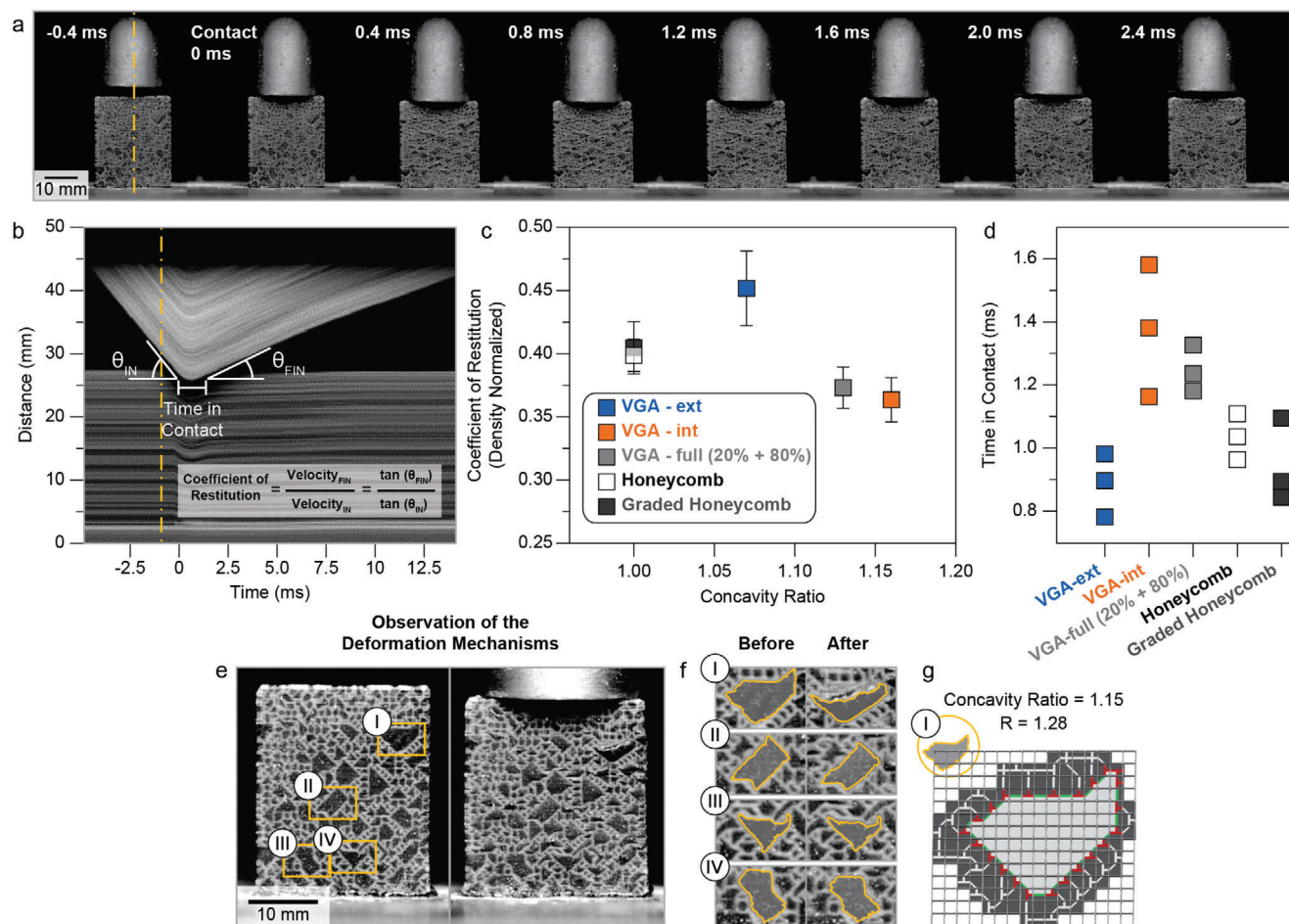
2405567 (6 of 9)

Figure 5. Drop tower testing. a) VGA-full samples before, during and after loading. b) Time versus distance of resliced striker/sample center axis with time in contact and angles giving striker initial and final velocities. c) Coefficient of restitution normalized for density for VGA-ext, VGA-int, VGA-full, and honeycomb polymer composite samples as a function of concavity ratio. d) Striker time in contact with sample for VGA-ext, VGA-int, VGA-full, and honeycomb polymer composite samples. e) VGA-full samples before and at maximum strain with highlighted large structural features. f) Highlighted large structural features before and at maximum strain. g) Coordination color coded tiling of largest structural feature.

defined as the ratio of the average striker velocity 2 ms before and after impact. The velocities are measured using the image processing software, FIJI,[52] by reslicing a vertical line through the center of each image (**Figure 5**a, vertical dashed line). Evaluating the evolution of pixel values over the experiment duration allows us to temporally track the striker position (Figure 5b). The VGA-generated samples are tested along with a periodic honeycomb sample and a 20% + 80% graded honeycomb sample, both with the same volume fraction of reinforcing phase as the 20% + 80% VGA-full sample, for comparison. After normalizing for density, we observe that the VGA-ext samples have the highest coefficient of restitution (0.45±0.03), indicating the least amount of energy dissipated (Figure 5c), along with the shortest time in contact (Figure 5d). Despite having the same volume fraction of reinforcing- and matrix phases, the VGA-full samples have a 7.5% lower coefficient of restitution (0.37±0.02) than their periodic equivalent (0.40±0.01), as well as a 16% longer time in contact, and a 9.8% lower coefficient of restitution (0.41±0.03) than their graded equivalent, as well as a 25% longer time in contact (Figure 5c,d). The similarity in behavior of the periodic honey-

comb and the graded honeycomb is because the branch thickness is always maintained, and there is a density difference of less than 10% between the two regions. We also test the 10% and 90% as well as 50% and 50% combination samples of external and internal regions to compare the coefficients of restitution (Figure S5, Supporting Information). To explain these differences in energy absorption, we observe a positive correlation between structural feature size, overall sample concavity and amount of deformation, noting that higher concavity leads to less constrained strut bending and buckling in the largest structural features (Figure 5e,f), like the large, compressible intercellular spaces of the orange pericarp, known for their energy dissipation.[15] The high percentages of low coordination tiles and consecutively repeating aligned tiles or two-tile combinations are responsible for the large size, while the connection of diagonal 2-R tiles with 3-R tiles are responsible for the high concavity (Figure 5g). Indeed, the largest structural features have local coordination numbers as low as 1.28 (Figure 5f,I) and concavity ratios as high as 1.17 (Figure 5f,IV). To quantify the strain and structural feature deformation, we can also refer back to the quasistatic 2D DIC maps

(Figure 3d–f), as well as the computational results (Figure 4e,g) which are valid also at our drop tower strain rate since the striker velocity is between 7 and 8 ms^{-1} and the elastic wave speed in the material is ≈575 ms^{-1}, indicating that drop tower loading occurs slowly enough to reach a state of stress equilibrium (Figure S7, Supporting Information).

2. Conclusions

We present a bioinspired material design method to achieve the desirable mechanical performances of irregular biological materials in synthetic materials. Instead of mimicking the biological structure one-to-one, our synthetic structures match the statistical distributions of features to obtain structure-to-property relationships similar to the biological material. Although this article only explores the irregular structure of the orange pericarp and its mechanical performance, the method is easily extendable to other irregular biological materials with desirable mechanical properties in 2D and 3D. Furthermore, this method lends itself to spatially-controlled bioinspired materials that combine the tiles and connectivity rules of multiple different materials simultaneously, to locally and globally tailor mechanical properties.

Supporting Information

Supporting Information is available from the Wiley Online Library or from the author.

Conflict of Interest

The authors declare no conflict of interest.

Data Availability Statement

The data that support the findings of this study are available from the corresponding author upon reasonable request.

[1] M. A. Meyers, A. Y. M. Lin, P. Y. Chen, J. Muyco, *J. Mech. Behav. Biomed. Mater.* **2008**, *1*, 76.

[2] T. M. Keaveny, E. F. Morgan, G. L. Niebur, O. C. Yeh, *Annu. Rev. Biomed. Eng.* **2003**, *3*, 307.

[3] T. Magrini, R. Libanori, A. Kan, A. R. Studart, *Rev. Bras. Ensino Fis.* **2021**, *43*, 20200438.

[4] A. P. J. Ackson, J. F. V. Vincent, R. M. T. Urner, *Proc. R. Soc. London, Ser. B* **1988**, *234*, 415.

[5] J. Chen, J. Xie, Z. Wu, E. M. A. Elbashiry, Y. Lu, *Mater. Sci. Eng., C* **2015**, *55*, 605.

[6] F. Barthelat, H. Tang, P. D. Zavattieri, C. M. Li, H. D. Espinosa, *J. Mech. Phys. Solids* **2007**, *55*, 306.

[7] I. Jäger, P. Fratzl, *Biophys. J.* **2000**, *79*, 1737.

[8] F. Barthelat, R. Rabiei, *J. Mech. Phys. Solids* **2011**, *59*, 829.

[9] N. H. Hart, S. Nimphius, T. Rantalainen, A. Ireland, A. Siafarikas, R. U. Newton, *J. Musculoskelet Neuronal Interact.* **2017**, *17*, 114.

[10] R. Oftadeh, M. Perez-Viloria, J. C. Villa-Camacho, A. Vaziri, A. Nazarian, *J. Biomech. Eng.* **2015**, *137*, 0108021.

[11] M. Thielen, T. Speck, R. Seidel, *J. Mater. Sci.* **2013**, *48*, 3469.

[12] M. Thielen, T. Speck, R. Seidel, *J. Mater. Sci.* **2014**, *49*, 43.

[13] S. Kamat, X. Su, R. Ballarini, A. H. Heuer, *Nature* **2000**, *405*, 1036.

[14] M. Jentzsch, S. Becker, M. Thielen, T. Speck, *Plants* **2022**, *11*, 991.

[15] M. Jentzsch, V. Albiez, T. C. Kardamakis, T. Speck, *Soft Matter* **2024**, *20*, 2804.

[16] T. Magrini, A. Senol, R. Style, F. Bouville, A. R. Studart, *J. Mech. Phys. Solids* **2022**, *159*, 104750.

[17] T. Magrini, F. Bouville, A. Lauria, H. Le Ferrand, T. P. Niebel, A. R. Studart, *Nat. Commun.* **2019**, *10*, 2794.

[18] F. Li, C. Yu, J. Zhong, C. Zhao, *Mech. Adv. Mater. Struct.* **2024**, *31*, 1071.

[19] G. X. Gu, M. Takaffoli, M. J. Buehler, *Adv. Mater.* **2017**, *29*, 1700060.

[20] F. Bouville, E. Maire, S. Meille, B. Van De Moortèle, A. J. Stevenson, S. Deville, *Nat. Mater.* **2014**, *13*, 508.

[21] S. Lee, D. D. Lim, E. Pegg, G. X. Gu, *Cell Rep. Phys. Sci.* **2022**, *3*, 101152.

[22] M. Li, N. Zhao, M. Wang, X. Dai, H. Bai, *Adv. Funct. Mater.* **2022**, *32*, 2205309.

[23] D. Gao, P. Chen, G. Lu, H. Yang, *Mater. Today Commun.* **2023**, *35*, 106031.

[24] H. Jiang, Y. Ren, Q. Jin, G. Zhu, Y. Hu, F. Cheng, *Thin-Walled Struct.* **2020**, *154*, 106911.

[25] H. Dai, W. Dai, Z. Hu, W. Zhang, G. Zhang, R. Guo, *Adv. Sci.* **2023**, *10*, 2207192.

[26] N. Kumar, A. Kumar, P. Uniyal, B. Ramalingaiah, S. Sharma, V. G. Goni, S. Aggarwal, S. K. Bhadada, B. Bhushan, *Philos. Trans. R. Soc., A* **2020**, *378*, 20190448.

[27] A. Mao, N. Zhao, Y. Liang, H. Bai, *Adv. Mater.* **2021**, *33*, 2007348.

[28] S. F. Fischer, M. Thielen, R. R. Loprang, R. Seidel, C. Fleck, T. Speck, A. Bührig-Polaczek, *Adv. Eng. Mater.* **2010**, *12*, B658.

[29] S. F. Fischer, M. Thielen, P. Weiß, R. Seidel, T. Speck, A. Bührig-Polaczek, M. Bünck, *J. Mater. Sci.* **2014**, *49*, 43.

[30] K. Liu, R. Sun, C. Daraio, *Science* **2022**, *377*, 975.

[31] T. Magrini, C. Fox, A. Wihardja, A. Kolli, C. Daraio, *Adv. Mater.* **2023**, *36*, 2305198.

[32] H. X. Zhu, A. H. Windle, *Acta Mater.* **2002**, *50*, 1041.

[33] H. X. Zhu, J. R. Hobdell, A. H. Windle, *Acta Mater.* **2000**, *48*, 4893.

[34] K. Li, X. L. Gao, J. Wang, *Int. J. Solids Struct.* **2007**, *44*, 5003.

[35] H. Rhee, M. T. Tucker, W. R. Whittington, M. F. Horstemeyer, H. Lim, *Sci. Eng. Compos. Mater.* **2015**, *22*, 365.

[36] M. Bianchi, F. Scarpa, C. W. Smith, *Acta Mater.* **2010**, *58*, 858.

[37] J. A. Carpenter, Z. Saraw, A. Schwegler, T. Magrini, G. Kuhn, A. Rafsanjani, A. R. Studart, J. A. Carpenter, Z. Saraw, A. Schwegler, T. Magrini, A. R. Studart, G. Kuhn, A. Rafsanjani, *Adv. Mater.* **2023**, *35*, 2207181.

[38] A. Dutto, M. Zanini, E. Jeoffroy, E. Tervoort, S. A. Mhatre, Z. B. Seibold, M. Bechthold, A. R. Studart, A. Dutto, E. Tervoort, A. R.

Studart, M. Zanini, E. Jeoffroy, S. A. Mhatre, Z. B. Seibold, M. Bechthold, *Adv. Mater. Technol.* **2023**, *8*, 2201109

[39] Z. Zhuang, Z. Qian, X. Wang, X. Xu, B. Chen, G. Song, X. Liu, L. Ren, L. Ren, *Adv. Sci.* **2023**, *11*, 2304947.

[40] J. Zhao, M. Li, J. Chen, W. Gao, H. Bai, *Nano Res.* **2023**, *17*, 679.

[41] F. M. Scott, K. C. Baker, *Bot. Gaz.* **1947**, *108*, 459.

[42] W. J. Whitehouse, *J. Microsc.* **1974**, *101*, 153.

[43] H. Zhao, Y. Han, C. Pan, D. Yang, H. Wang, T. Wang, X. Zeng, P. Su, *Micromachines* **2021**, *12*, 664.

[44] M. F. Thorpe, *J. Non. Cryst Solids* **1983**, *57*, 355.

[45] H. Lu, T.-U. Lee, J. Ma, Y. M. Xie, *Eng. Struct.* **2024**, *304*, 117686.

[46] M. Doškář, J. Zeman, D. Jarušková, J. Novák, *Eur. J. Mech. A: Solids* **2018**, *70*, 280.

[47] Z. Chen, A. Ogren, C. Daraio, L. C. Brinson, C. Rudin, *Extreme Mech. Lett.* **2022**, *57*, 101895.

[48] T. Li, Y. Li, *Adv. Mater.* **2024**, *36*, 2309604.

[49] J. Jung, A. Chen, G. X. Gu, *Mater. Today* **2024**, *73*, 1.

[50] H. Pahlavani, K. Tsifoutis-Kazolis, M. C. Saldivar, P. Mody, J. Zhou, M. J. Mirzaali, A. A. Zadpoor, H. Pahlavani, K. Tsifoutis-Kazolis, M. C. Saldivar, J. Zhou, M. J. Mirzaali, A. A. Zadpoor, P. Mody, *Adv. Mater.* **2024**, *36*, 2303481.

[51] M. Jentzsch, M. C. Badstöber, F. Umlas, T. Speck, *Front. Mater.* **2022**, *9*, 979151.

[52] C. A. Schneider, W. S. Rasband, K. W. Eliceiri, *Nat. Methods* **2012**, *9*, 671.

[53] I. Arganda-Carreras, R. Fernández-González, A. Muñoz-Barrutia, C. Ortiz-De-Solorzano, *Microsc. Res. Tech.* **2010**, *73*, 1019.

[54] J. R. C. Dizon, A. H. Espera, Q. Chen, R. C. Advincula, *Addit. Manuf.* **2018**, *20*, 44.

[55] D. Bell, T. Siegmund, *Addit. Manuf.* **2018**, *21*, 658.

[56] V. Slesarenko, S. Rudykh, *Int. J. Eng. Sci.* **2018**, *123*, 62.

[57] V. S. Deshpande, M. F. Ashby, N. A. Fleck, *Acta Mater.* **2001**, *49*, 1035.

[58] C. R. Calladine, *Int. J. Solids Struct.* **1978**, *14*, 161.

[59] J. C. Maxwell, *J. Sci.* **1864**, *27*, 294.